Sequence-Impedance-Based Stability Comparison between VSGs and Traditional Grid-Connected Inverters

Wu, Wenhua; Zhou, Leming; Chen, Yandong; Luo, An; Dong, Yanting; Zhou, Xiaoping; Xu, Qianming; Yang, Ling; Guerrero, Josep M.

Published in:
IEEE Transactions on Power Electronics

DOI (link to publication from Publisher):
10.1109/TPEL.2018.2841371

Publication date:
2019

Document Version
Accepted author manuscript, peer reviewed version

Citation for published version (APA):
Wu, W., Zhou, L., Chen, Y., Luo, A., Dong, Y., Zhou, X., Xu, Q., Yang, L., & Guerrero, J. M. (2019). Sequence-Impedance-Based Stability Comparison between VSGs and Traditional Grid-Connected Inverters. *IEEE Transactions on Power Electronics*, *34*(1), 46-52. Article 8368151. https://doi.org/10.1109/TPEL.2018.2841371

This article has been accepted for publication in a future issue of this journal, but has not been fully edited. Content may change prior to final publication. Citation information: DOI 10.1109/TPEL.2018.2841371, IEEE Transactions on Power Electronics

Sequence-Impedance-Based Stability Comparison between VSGs and Traditional Grid-Connected Inverters

Wenhua Wu, *Student Member, IEEE*, Leming Zhou, *Member, IEEE*, Yandong Chen, *Member, IEEE*, An Luo, *Senior Member, IEEE*, Yanting Dong, Xiaoping Zhou, *Student Member, IEEE*, Qianming Xu, *Member, IEEE*, Ling Yang, *Student Member, IEEE*, Josep M. Guerrero, *Fellow, IEEE*

***Abstract*—Traditional grid-connected inverters (TGCI) could suffer from small-signal instability owing to the dynamic interactions among inverters and a weak grid. In this letter, the small-signal sequence impedance model of the virtual synchronous generator (VSG) is built, and the sequence impedance characteristics of the VSG and the TGCI are compared and analyzed. The sequence impedance of the TGCI is mainly capacitive in the middle-frequency area, and the impedance amplitude is quite high. By contrast, the sequence impedance of the VSG, being consistent with the grid impedance characteristics, is generally inductive, and the impedance amplitude is quite low. Based on the sequence impedance model and the Nyquist stability criterion, the influence of the grid stiffness, number of paralleled inverters, and phase-locked loop (PLL) bandwidth on the stability of the VSG and the TGCI grid-connected system is analyzed. The stability analysis results show that the TGCI loses stability easily whereas the VSG still works well without PLL restrictions under an ultra-weak grid or with a large number of inverters connected to the grid. Therefore, the VSG is more suitable than the TGCI for achieving high penetration of renewable energy generation in an ultra-weak grid from a system stability viewpoint. Finally, experimental results validate the sequence impedance model and the stability analysis.**

***Index Terms*—Virtual synchronous generator; harmonic oscillation; sequence impedance modeling; ultra-weak grid.**

I. Introduction

In recent years, renewable energy generation has developed rapidly owing to increasing fossil fuel shortage and environmental pollution. At present, renewable energy generation is mainly located in remote areas such as deserts, mountainous regions, and islands. Therefore, it is weakly connected to the grid with high impedance [1]. A traditional grid-connected inverter (TGCI) often adopts output current feed-forward decoupling control [2] in which the inverter is controlled as a current source. TGCIs can cause small-signal instability problems owing to the dynamic interaction among inverters and the weak grid [2]. As the number of inverters increases, this problem becomes more serious, thus hindering the large-scale development and application of renewable energy generation.

The impedance-based approach is widely used to analyze the interaction stability of TGCIs [2]-[3]. In [2], an output impedance model was built for a grid-connected inverter *in synchronous rotating reference frames* (SRRFs), and the influence of the phase-locked loop (PLL) on system stability was studied. The larger the PLL bandwidth, the faster is the system dynamic response but the worse is the system stability. In [3], a sequence impedance model was built for a grid-connected inverter *in stationary reference frames* (SRFs). The sequence impedance is capacitive in the middle-frequency area and tends to couple with the grid inductance, thus leading to instability. To mitigate the instability of the grid-connected inverter system, the PLL bandwidth should be lowered [4] or active damping control should be used to reshape the inverter impedance [5]. Other studies analyzed the stability of power synchronization control [6] and advanced vector control [7]. These were demonstrated to be excellent control methods for inverters connected to a weak grid.

The virtual synchronous generator (VSG) imitates the external characteristics of a synchronous generator and provides the necessary frequency and voltage support for a weak grid [8]-[13]. Its output characteristic is equivalent to that of the voltage source; this is essentially different from TGCI. A small-signal model for the power loop of a VSG was established, and a step-by-step parameter design method that considered the stability and dynamic performance of the VSG was proposed [10]-[11]. However, studies have not yet examined the interaction stability of the VSG and the weak grid. In [12]-[13], a small-signal time-domain state space model of the VSG was built in SRRFs. However, the VSG can be controlled either in SRRFs [12] or in SRFs [8]. When the VSG is controlled in SRFs, its output voltage and current are alternating time variables with no dc operation point. Therefore, it is difficult to apply the traditional time-domain linearization method to the VSG controlled in SRFs. If SRRFs are fabricated for traditional small-signal linearization modeling, the physical meaning of the impedance model will become confusing.

The premise that the VSG can actively support the grid is based on the fact that the VSG can operate steadily. In this letter, first, the sequence impedance model of the VSG in SRFS is built by using the harmonic linearization method, and the impedance characteristics of the VSG and TGCI are compared and analyzed. Then, the influence of different parameters on the stability of the VSG and TGCI is studied. From a system stability viewpoint, the VSG is shown to be more preferable than the TGCI in an ultra-weak grid or in high penetration of renewable energy generation. Finally, the experimental results validate the sequence impedance model and stability analysis.

II. Topology and Control Scheme of the VSG

Fig. 1 shows the topology and control scheme of the VSG [8]. V_{dc} is the dc-side voltage of the VSG, and it can be regarded as a

This work was supported in part by the National Key Research and Development Program of China under Grant 2017YFB0902000, in part by the State Grid Science and Technology Project under Grant SGXJ0000KXJS1700841, and in part by the Natural Science Foundation of China (NSFC) under Grant 51577056.

W. Wu, L. Zhou, Y. Chen, A. Luo, X. Zhou, Q. Xu, and L. Yang are with the College of Electrical and Information Engineering, Hunan University, Changsha 410082, China (e-mail: wenhua_5@163.com; leming_zhou@126.com; yandong_chen@hnu.edu.cn; an_luo@126.com; zxp2011@hnu.edu.cn; hnuxqm@foxmail.com; yangling_1992@163.com).

Y. Dong is with the Qingyuan Power Supply Bureau, Guangdong Power Grid Corporation, Qingyuan, China (KarenDongyt@163.com).

J. M. Guerrero is with the Department of Energy Technology, Aal-borg University, 9220 Aalborg East, Denmark (e-mail: joz@et.aau.dk).

constant value; e_a, e_b, and e_c are the inner electric potentials of the VSG; i_a, i_b, and i_c are the output currents of the VSG; v_a, v_b, and v_c are the output terminal voltages of the VSG; L_f, C_f, and R_f are the filter inductance, filter capacitance, and damping resistance, respectively; L_g and R_g are the equivalent inductance and resistance of the grid, respectively; R_{line} and L_{line} are the resistance and inductance of line between the VSG and the point of common coupling (PCC), respectively; and $Z_{g,p}(s)$ and $Z_{g,n}(s)$ are the positive- and negative-sequence impedance of the grid, respectively. Because the filter capacitance is not included in the VSG control system, it can be considered to be a part of the VSG or a part of the grid for impedance-based stability analysis. For simplifying the analysis, we define $Z_{g,p}(s) = Z_{g,n}(s) = (R_g + sL_g + R_{line} + sL_{line})//(R_f + 1/sC_f)$ for a single VSG connected to the PCC. When multiple VSGs are connected to the PCC, $Z_{g,p}(s) = Z_{g,n}(s) = (R_g + sL_g)$.

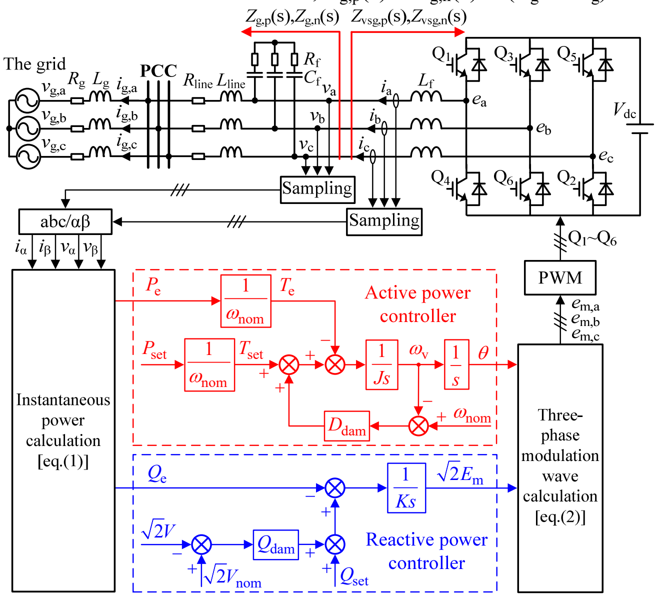

Fig. 1 Topology and control scheme of the VSG.

The active power controller of the VSG emulates the inertia and primary frequency regulation characteristics of the synchronous generator, and the reactive power controller emulates the primary voltage regulation characteristics of the synchronous generator. According to the instantaneous power theory, the output active power P_e and reactive power Q_e of the VSG can be calculated as follows:

$$\begin{cases} P_e = 1.5(v_\alpha i_\alpha + v_\beta i_\beta) \\ Q_e = 1.5(v_\beta i_\alpha - v_\alpha i_\beta) \end{cases} \tag{1}$$

The modulation wave of the VSG is determined by the active and reactive power controllers as follows:

$$\begin{cases} e_{m,a} = \sqrt{2}E_m \cos\theta \\ e_{m,b} = \sqrt{2}E_m \cos(\theta - 2\pi/3) \\ e_{m,c} = \sqrt{2}E_m \cos(\theta + 2\pi/3) \end{cases} \tag{2}$$

where E_m and θ are the RMS and phase angle of the three-phase modulation wave, respectively.

III. Sequence Impedance Modeling and Impedance Characteristics Analysis of the VSG

The VSG is controlled in SRFs, and therefore, it cannot be modeled in SRFs for traditional small-signal linearization. In this letter, the positive- and negative-sequence output impedance models of the VSG are built by applying the harmonic linearization method. In the time-domain, after adding small-signal perturbations, the phase A output voltage and output current of the VSG are as follows:

$$v_a(t) = V_1\cos(2\pi f_1 t) + V_p\cos(2\pi f_p t + \varphi_{v,p}) + V_n\cos(2\pi f_n t + \varphi_{v,n}) \tag{3}$$

$$i_a(t) = I_1\cos(2\pi f_1 t + \varphi_{i,1}) + I_p\cos(2\pi f_p t + \varphi_{i,p}) + I_n\cos(2\pi f_n t + \varphi_{i,n}) \tag{4}$$

where V_1, V_p, and V_n are the amplitude of the fundamental voltage, positive-sequence voltage perturbation, and negative-sequence voltage perturbation, respectively; I_1, I_p, and I_n are the amplitude of the fundamental current, positive-sequence current response, and negative-sequence current response, respectively; f_1, f_p, and f_n are the fundamental frequency, positive-sequence perturbation frequency, and negative-sequence perturbation frequency, respectively; $\varphi_{v,p}$ and $\varphi_{v,n}$ are the initial phase angle of the positive-sequence and negative-sequence voltage perturbation, respectively; $\varphi_{i,1}$, $\varphi_{i,p}$, and $\varphi_{i,n}$ are the initial phase angle of the fundamental current, positive-sequence current response, and negative-sequence current response, respectively. In the frequency-domain, v_a and i_a can be described as follows:

$$v_a[f] = \begin{cases} \mathbf{V}_1, & f = \pm f_1 \\ \mathbf{V}_p, & f = \pm f_p \\ \mathbf{V}_n, & f = \pm f_n \end{cases}, \quad i_a[f] = \begin{cases} \mathbf{I}_1, & f = \pm f_1 \\ \mathbf{I}_p, & f = \pm f_p \\ \mathbf{I}_n, & f = \pm f_n \end{cases} \tag{5}$$

where $\mathbf{V}_1 = V_1/2$, $\mathbf{V}_p = (V_p/2)e^{\pm j\varphi_{v,p}}$, $\mathbf{V}_n = (V_n/2)e^{\pm j\varphi_{v,n}}$, $\mathbf{I}_1 = (I_1/2)e^{\pm j\varphi_{i,1}}$, $\mathbf{I}_p = (I_p/2)e^{\pm j\varphi_{i,p}}$, and $\mathbf{I}_n = (I_n/2)e^{\pm j\varphi_{i,n}}$. The bold capital letters in the formula represent the frequency-domain representation of the signal, including the frequency, amplitude, and phase information of the signal.

From Fig. 1, the relationship among the inner electric potential, output terminal voltage, and output current of the VSG is as follows:

$$L_f \frac{d}{dt}\begin{bmatrix} i_a & i_b & i_c \end{bmatrix}^T = \begin{bmatrix} e_a & e_b & e_c \end{bmatrix}^T - \begin{bmatrix} v_a & v_b & v_c \end{bmatrix}^T \tag{6}$$

The frequency-domain expressions of the output terminal voltage and output current of the VSG in α-β reference frames can be obtained as follows:

$$v_\alpha[f] = \begin{cases} \mathbf{V}_1, f = \pm f_1 \\ \mathbf{V}_p, f = \pm f_p \\ \mathbf{V}_n, f = \pm f_n \end{cases}, \quad v_\beta[f] = \begin{cases} \mp j\mathbf{V}_1, f = \pm f_1 \\ \mp j\mathbf{V}_p, f = \pm f_p \\ \pm j\mathbf{V}_n, f = \pm f_n \end{cases} \tag{7}$$

$$i_\alpha[f] = \begin{cases} \mathbf{I}_1, f = \pm f_1 \\ \mathbf{I}_p, f = \pm f_p \\ \mathbf{I}_n, f = \pm f_n \end{cases}, \quad i_\beta[f] = \begin{cases} \mp j\mathbf{I}_1, f = \pm f_1 \\ \mp j\mathbf{I}_p, f = \pm f_p \\ \pm j\mathbf{I}_n, f = \pm f_n \end{cases} \tag{8}$$

By substituting (7) and (8) into (1) and applying the frequency-domain convolution theorem, the expression of the active power in the frequency-domain can be obtained as follows:

$$P_e[f] = \begin{cases} 3(\mathbf{V}_1\mathbf{I}_1^* + \mathbf{V}_1^*\mathbf{I}_1 + \mathbf{V}_p\mathbf{I}_p^* + \mathbf{V}_p^*\mathbf{I}_p + \mathbf{V}_n\mathbf{I}_n^* + \mathbf{V}_n^*\mathbf{I}_n), \mathrm{dc} \\ 3(\mathbf{V}_1^*\mathbf{I}_p + \mathbf{V}_p\mathbf{I}_1^*), & f = \pm(f_p - f_1) \\ 3(\mathbf{V}_1\mathbf{I}_n + \mathbf{V}_n\mathbf{I}_1), & f = \pm(f_n + f_1) \\ 3(\mathbf{V}_p\mathbf{I}_n + \mathbf{V}_n\mathbf{I}_p), & f = \pm(f_p + f_n) \end{cases} \tag{9}$$

where * denotes complex conjugation.

According to the active power controller of the VSG in Fig. 1, the expression of θ can be obtained as follows:

$$\theta = M(s)(\omega_{nom}D_{dam} + P_{set}/\omega_{nom} - P_e/\omega_{nom}) \tag{10}$$

where $M(s) = 1/(Js^2 + D_{dam}s)$, J is the virtual moment of inertia, ω_{nom} is the rated angular frequency, D_{dam} is the damping coefficient, and P_{set} is the active power reference.

By substituting (9) into (10) and neglecting terms proportional to second-order perturbations, the expression of θ in the frequency-domain is as follows:

This article has been accepted for publication in a future issue of this journal, but has not been fully edited. Content may change prior to final publication. Citation information: DOI 10.1109/TPEL.2018.2841371, IEEE Transactions on Power Electronics

$$\theta[f]=\begin{cases}M(s)\left[\omega_{\mathrm{nom}}D_{\mathrm{dam}}+P_{\mathrm{set}}/\omega_{\mathrm{nom}}-3(\mathbf{V}_1\mathbf{I}_1^*+\mathbf{V}_1^*\mathbf{I}_1)/\omega_{\mathrm{nom}}\right], & \mathrm{dc}\\ -3M(s)(\mathbf{V}_1^*\mathbf{I}_{\mathrm{p}}+\mathbf{V}_{\mathrm{p}}\mathbf{I}_1^*)/\omega_{\mathrm{nom}}, & f=\pm(f_{\mathrm{p}}-f_1)\\ -3M(s)(\mathbf{V}_1\mathbf{I}_{\mathrm{n}}+\mathbf{V}_{\mathrm{n}}\mathbf{I}_1)/\omega_{\mathrm{nom}}, & f=\pm(f_{\mathrm{n}}+f_1)\end{cases} \quad (11)$$

The phase angle perturbation $\Delta\theta$ is introduced into the phase angle θ of the three-phase modulation wave of the VSG, that is, $\theta = \theta_1 + \Delta\theta$. θ_1 is the phase angle of the fundamental voltage. According to (11), the expression of $\Delta\theta$ in the frequency-domain is as follows:

$$\Delta\theta[f]=\begin{cases}-3M(s)(\mathbf{V}_1^*\mathbf{I}_{\mathrm{p}}+\mathbf{V}_{\mathrm{p}}\mathbf{I}_1^*)/\omega_{\mathrm{nom}}, & f=\pm(f_{\mathrm{p}}-f_1)\\ -3M(s)(\mathbf{V}_1\mathbf{I}_{\mathrm{n}}+\mathbf{V}_{\mathrm{n}}\mathbf{I}_1)/\omega_{\mathrm{nom}}, & f=\pm(f_{\mathrm{n}}+f_1)\end{cases} \quad (12)$$

Because $\Delta\theta$ is a small perturbation, $\cos\theta$ can be obtained as

$$\cos\theta=\cos(\theta_1+\Delta\theta)\approx\cos\theta_1-\Delta\theta\sin\theta_1 \quad (13)$$

Based on (12), (13), and the frequency-domain convolution theorem and ignoring the nonlinear coupling at $\pm(f_{\mathrm{p}}-2f_1)$ and $\pm(f_{\mathrm{n}}+2f_1)$, the relationship among the voltage perturbation, current perturbation, and $\cos\theta[f]$ can be expressed as

$$\cos\theta[f]=\begin{cases}-1.5e^{\pm j\varphi_{\mathrm{vir}}}M(s\mp j2\pi f_1)(\mathbf{V}_1^*\mathbf{I}_{\mathrm{p}}+\mathbf{V}_{\mathrm{p}}\mathbf{I}_1^*)/\omega_{\mathrm{nom}}, & f=\pm f_{\mathrm{p}}\\ -1.5e^{\mp j\varphi_{\mathrm{vir}}}M(s\pm j2\pi f_1)(\mathbf{V}_1\mathbf{I}_{\mathrm{n}}+\mathbf{V}_{\mathrm{n}}\mathbf{I}_1)/\omega_{\mathrm{nom}}, & f=\pm f_{\mathrm{n}}\end{cases} \quad (14)$$

where $\varphi_{\mathrm{vir}} = \arcsin(P_{\mathrm{e}}\omega_{\mathrm{nom}}L_{\mathrm{f}}/E_{\mathrm{m}}V_1) + \pi/2$; $\arcsin(P_{\mathrm{e}}\omega_{\mathrm{nom}}L_{\mathrm{f}}/E_{\mathrm{m}}V_1)$ is the power-angle of the VSG.

The amplitude of the fundamental wave in $\cos\theta[f]$ is much smaller than the amplitude of the dc component in $\sqrt{2}E_{\mathrm{m}}[f]$ (a difference of two orders of magnitude). Therefore, the output of the reactive power controller of the VSG can be assumed to be constant in the steady state for small-signal modeling. Based on (2) and (14) and considering the influence of the sampling delay, PWM delay, and low-pass filter, the frequency-domain expression of $e_{\mathrm{m,a}}$ can be obtained as follows:

$$e_{\mathrm{m,a}}[f]=\begin{cases}-1.5K(s)e^{\pm j\varphi_{\mathrm{vir}}}M(s\mp j2\pi f_1)(\mathbf{V}_1^*\mathbf{I}_{\mathrm{p}}+\mathbf{V}_{\mathrm{p}}\mathbf{I}_1^*)/\omega_{\mathrm{nom}}, & f=\pm f_{\mathrm{p}}\\ -1.5K(s)e^{\mp j\varphi_{\mathrm{vir}}}M(s\pm j2\pi f_1)(\mathbf{V}_1\mathbf{I}_{\mathrm{n}}+\mathbf{V}_{\mathrm{n}}\mathbf{I}_1)/\omega_{\mathrm{nom}}, & f=\pm f_{\mathrm{n}}\end{cases} \quad (15)$$

where $K(s) = \sqrt{2}E_{\mathrm{m}}e^{-1.5T_{\mathrm{s}}s}/[(1 + s/\omega_{\mathrm{v}})(1 + s/\omega_{\mathrm{i}})]$; ω_{v} and ω_{i} are the cut-off angular frequency of the low-pass filter for the voltage and current signal, respectively; and T_{s} is the switching period.

By substituting (15) into (6), the positive- and negative-sequence impedances of the VSG can be obtained as follows:

$$Z_{\mathrm{vsg,p}}(s)=-\frac{V_{\mathrm{p}}(s)}{I_{\mathrm{p}}(s)}=\frac{0.75V_1M(s-j2\pi f_1)K(s)e^{j\varphi_{\mathrm{vir}}}/\omega_{\mathrm{nom}}+sL_{\mathrm{f}}}{1+0.75I_1M(s-j2\pi f_1)K(s)e^{j(\varphi_{\mathrm{vir}}-\varphi_{\mathrm{i,1}})}/\omega_{\mathrm{nom}}} \quad (16)$$

$$Z_{\mathrm{vsg,n}}(s)=-\frac{V_{\mathrm{n}}(s)}{I_{\mathrm{n}}(s)}=\frac{0.75V_1M(s+j2\pi f_1)K(s)e^{-j\varphi_{\mathrm{vir}}}/\omega_{\mathrm{nom}}+sL_{\mathrm{f}}}{1+0.75I_1M(s+j2\pi f_1)K(s)e^{j(\varphi_{\mathrm{i,1}}-\varphi_{\mathrm{vir}})}/\omega_{\mathrm{nom}}} \quad (17)$$

TABLE I. SYSTEM PARAMETERS OF THE VSG

Parameters	Values	Parameters	Values	Parameters	Values
V_{dc}/V	700	L_{line}/mH	0.024	E_{m}/V	220
V_{nom}/V	220	R_{line}/Ω	0.05	f_1/Hz	50
L_{f}/mH	3	P_{set}/kW	10	$f_{\mathrm{s}}(1/T_{\mathrm{s}})$/kHz	20
C_{f}/μF	20	Q_{set}/kVar	0	ω_{nom}/(rad/s)	314.159
R_{f}/Ω	1.5	D_{dam}	5	J/(kg·m²)	0.057
L_{g}/mH	4	Q_{dam}	321	ω_{v}/(rad/s)	2π·4000
R_{g}/Ω	0.2	K	7.1	ω_{i}/(rad/s)	2π·4000

Table I shows the system parameters of the VSG; the control parameters of the VSG are designed with reference to [10]. Fig. 2 shows the frequency response characteristics of the positive- and negative-sequence impedances of the VSG and their simulation measurement results. This figure indicates that the impedance measurement results show good agreement with the built impedance model, thus validating the VSG sequence impedance modeling.

The TGCI usually adopts output current feed-forward decoupling control in SRFs [3]; the detailed control block diagram and control parameters are shown in Fig. 11 in the Appendix. The sequence impedance model of the TGCI was reported in [3]. Fig. 3 shows the frequency response characteristics of the positive- and negative-sequence impedances of the TGCI and their simulation measurement results. In Fig. 3, $Z_{\mathrm{inv,p}}(s)$ and $Z_{\mathrm{inv,n}}(s)$ are the positive- and negative-sequence impedance of the TGCI, respectively.

From Fig. 2 and Fig. 3, the sequence impedance characteristics of the VSG and TGCI are compared as follows:

(1) In the low- and middle-frequency areas, the impedance amplitude of the VSG is far lower than that of the TGCI. This is because the VSG is controlled as a voltage source, and the equivalent output impedance is small. By contrast, the TGCI is controlled as a current source, and the equivalent output impedance is large.

(2) The sequence impedance of the VSG is basically inductive because the VSG has the external characteristics of a synchronous generator. In the low- and middle-frequency areas, the sequence impedance of the VSG is generally consistent with the impedance characteristic of the grid. By contrast, in the middle-frequency area, the sequence impedance of the TGCI is mainly capacitive, making it easy to couple with the grid inductance and thereby cause instability.

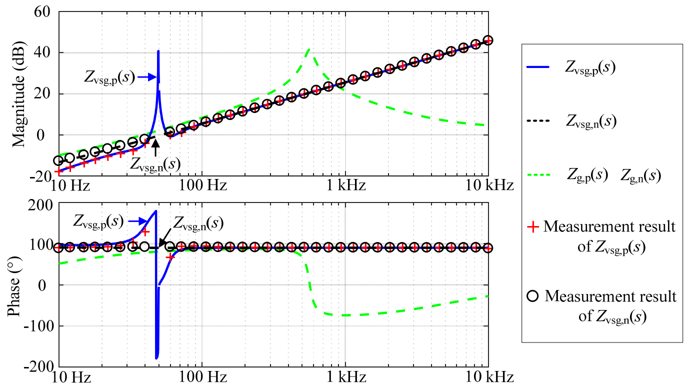

Fig. 2 Sequence impedances of the VSG and their simulation measurement results.

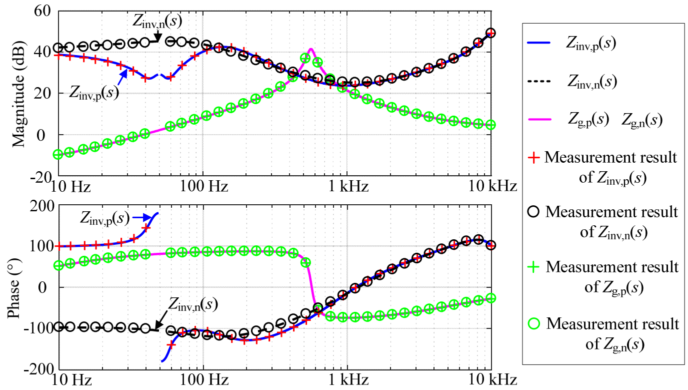

Fig. 3 Sequence impedances of the TGCI and their simulation measurement results.

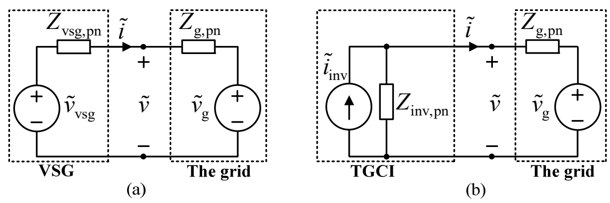

Fig. 4 Small-signal representation of the grid-connected inverter system. (a) Thévenin equivalent circuit of the VSG system; (b) Norton equivalent circuit of the TGCI system.

IV. STABILITY COMPARISON BETWEEN THE VSG AND THE TGCI

Fig. 4 shows the small-signal description of the VSG and the TGCI grid-connected systems. The impedance ratio of the grid-connected inverter system is usually used for the Nyquist stability

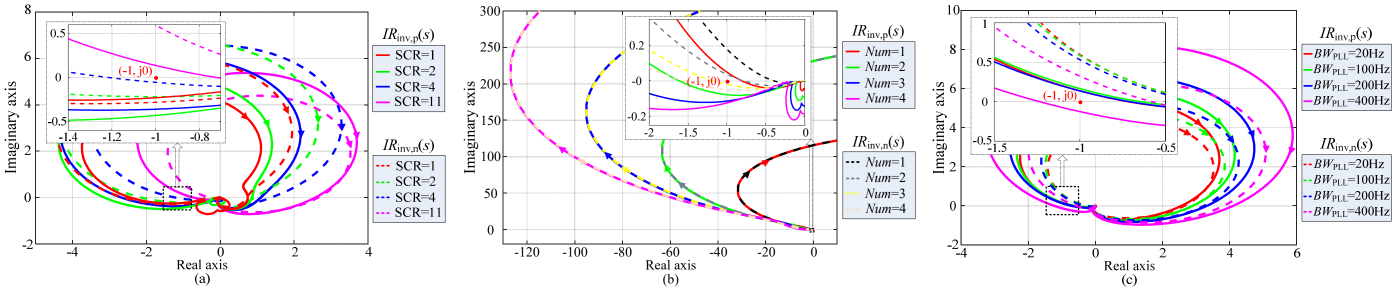

Fig. 5 Nyquist Plots of impedance ratios $IR_{inv,p}(s)$ and $IR_{inv,n}(s)$ of the TGCI with different parameters. (a) Different SCRs; (b) Different number of paralleled TGCIs; (c) Different PLL bandwidths.

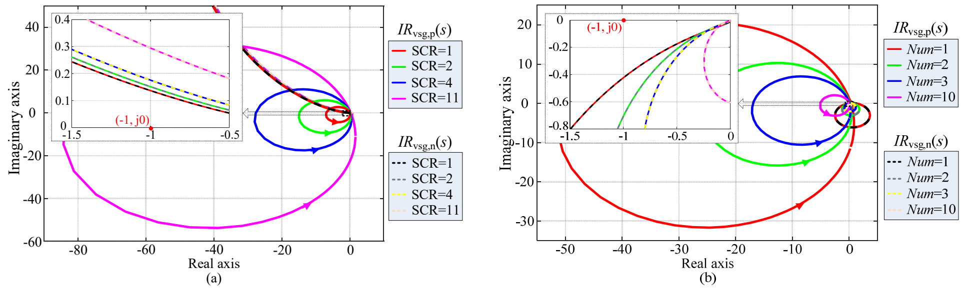

Fig. 6 Nyquist plots of impedance ratios $IR_{vsg,p}(s)$ and $IR_{vsg,n}(s)$ of the VSG with different parameters. (a) Different SCRs; (b) Different number of paralleled VSGs.

criterion. The external characteristics of the VSG can be regarded as a voltage source. From Fig. 4(a), the grid-connected current expression of the VSG is as follows:

$$\tilde{i} = \frac{\tilde{v}_{vsg} - \tilde{v}_g}{Z_{vsg,pn} + Z_{g,pn}} = (\tilde{v}_{vsg} - \tilde{v}_g)\frac{1}{Z_{g,pn}}\frac{1}{1 + Z_{vsg,pn}/Z_{g,pn}} \tag{18}$$

Here, $\tilde{v}_{vsg}$ is the ideal voltage source of the Thévenin equivalent circuit of the VSG, which is stable. The voltage of the ideal grid, $\tilde{v}_g$, is also stable. Because the grid admittance acts passively, that is, the real part of the admittance is nonnegative [14], $1/Z_{g,pn}$ is stable. According to (18), whether the VSG-grid system is stable depends on $1/(1 + Z_{vsg,pn}/Z_{g,pn})$.

Therefore, the impedance ratio used to study stability of the VSG is the VSG output impedance divided by the grid impedance, as shown in (19). By contrast, the external characteristics of the TGCI can be regarded as a current source; in this case, the impedance ratio is the grid impedance divided by the TGCI output impedance [15], as shown in (20).

$$IR_{vsg,p}(s) = Z_{vsg,p}(s)/Z_{g,p}(s),\quad IR_{vsg,n}(s) = Z_{vsg,n}(s)/Z_{g,n}(s) \tag{19}$$

$$IR_{inv,p}(s) = Z_{g,p}(s)/Z_{inv,p}(s),\quad IR_{inv,n}(s) = Z_{g,n}(s)/Z_{inv,n}(s) \tag{20}$$

The grid weakness is distinguished by the short circuit ratio (SCR), that is, SCR = S_{SC}/S_N where S_{SC} is the short-circuit capacity at the PCC, and S_N is the rated capacity of the grid-connected inverters. In this letter, S_N is 10 kVA when a single grid-connected inverter is connected to the PCC.

Fig. 5 shows the Nyquist plots of the impedance ratios $IR_{inv,p}(s)$ and $IR_{inv,n}(s)$ of the TGCI with different parameters. The poles of $IR_{inv,p}(s)$ and $IR_{inv,n}(s)$ are both not in the right half-plane (RHP). In this figure, *Num* and BW_{PLL} represent the number of paralleled TGCIs and the PLL bandwidth, respectively. From Fig. 5(a), when the grid is weaker, the Nyquist plots more easily encircle the critical point (−1, j0) and the system is more unstable. When SCR ≤ 4, the Nyquist plots encircle (−1, j0) and the system is unstable. From Fig. 5(b), the Nyquist plot moves toward the left with increasing number of TGCIs, indicating that the system stability deteriorates. When *Num* ≥ 2, the impedance ratio does not satisfy the Nyquist stability criterion and the system is unstable. From Fig. 5(c), the PLL bandwidth greatly influences the system stability; specifically, when BW_{PLL} increases, the system becomes more unstable, and when BW_{PLL} ≥ 400 Hz, the Nyquist plots encircle (−1, j0) and the system is unstable.

The analysis in Fig. 5 indicates that the TGCI shows poor adaptability to a weak grid and that the system stability is greatly influenced by the number of paralleled TGCIs and the PLL bandwidth. Therefore, the TGCI is difficult to achieve high penetration renewable energy generation in a weak grid from a system stability viewpoint.

Fig. 6 shows the Nyquist plots of the impedance ratios $IR_{vsg,p}(s)$ and $IR_{vsg,n}(s)$ of the VSG with different parameters. $IR_{vsg,p}(s)$ has two poles in the RHP, and $IR_{vsg,n}(s)$ has no poles in the RHP. Therefore, when the system is stable, the Nyquist plots of $IR_{vsg,p}(s)$ should cross the negative real axis at the right side of (−1, j0) once in the counterclockwise direction and those of $IR_{vsg,n}(s)$ cannot encircle (−1, j0). From Fig. 6, irrespective of whether the grid becomes weaker or the number of VSGs increases, the Nyquist plots of $IR_{vsg,p}(s)$ cross the negative real axis at the right side of (−1, j0) once in the counterclockwise direction and those of $IR_{vsg,n}(s)$ do not encircle (−1, j0). Therefore, VSG is more adaptable to a weak grid, and the system remains stable when the VSG penetration is high. In addition, the VSG, like a synchronous generator, does not need the PLL and consequently cannot be affected by the PLL. Therefore, the VSG can effectively solve stability issues, making it suitable for achieving high penetration of renewable energy generation in an ultra-weak grid (SCR ⩽ 2) from a system stability viewpoint.

V. Experimental Results

To validate the sequence impedance model of the VSG and the stability analysis, experimental platforms for an impedance measurement system and a grid-connected renewable energy generation system are built, as shown in Fig. 7. The impedance measurement system shown in Fig. 7(a) uses a programmable ac source (Chroma 61611) to inject the voltage perturbation. Because of the limit of the output ac voltage frequency and the difficulty in extracting the disturbance signal near the fundamental frequency, the range of impedance measurements in the experiment is 15–45 Hz and 55 Hz to 1.5 kHz. In Fig. 7(b), VSGs and traditional grid-connected inverters share the same hardware circuit. Their control schemes are implemented in TI DSP TMS320F2812. All inverters are connected to the PCC. The experimental parameters are the same as those in the previous analysis.

This article has been accepted for publication in a future issue of this journal, but has not been fully edited. Content may change prior to final publication. Citation information: DOI 10.1109/TPEL.2018.2841371, IEEE Transactions on Power Electronics

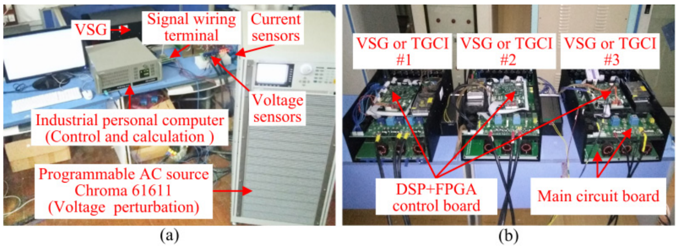

Fig. 7 Experimental platform. (a) Test system for ac impedance measurement; (b) Grid-connected renewable energy generation with three inverters.

Fig. 8 shows the experimental results of the sequence impedance measurement for the VSG. These results indicate that the experimental measurement results show good agreement with the built impedance model, thus validating the VSG sequence impedance modeling.

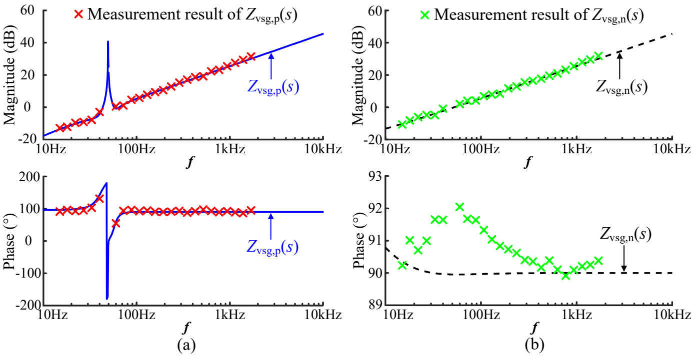

Fig. 8 Experimental results of sequence impedance measurement for the VSG. (a) Measurement results of $Z_{vsg,p}(s)$; (b) Measurement results of $Z_{vsg,n}(s)$.

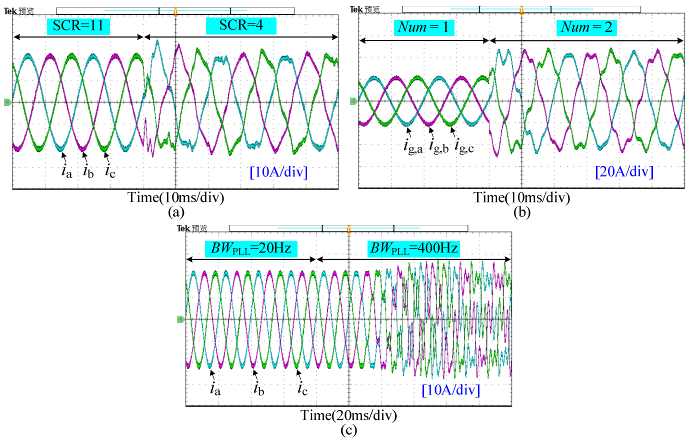

Fig. 9 Experimental results of TGCIs under different conditions. (a) SCR is decreased from 11 to 4; (b) *Num* is increased from 1 to 2; (c) BW_{PLL} is increased from 20 to 400 Hz.

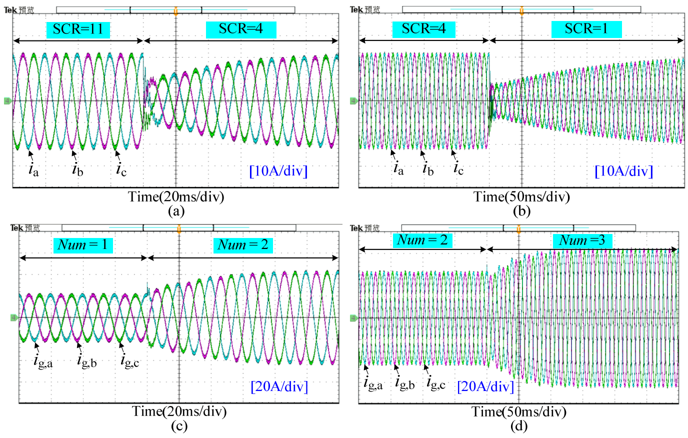

Fig. 10 Experimental results of VSGs under different conditions. (a) SCR is decreased from 11 to 4; (b) SCR is decreased from 4 to 1; (c) *Num* is increased from 1 to 2; (d) *Num* is increased from 2 to 3.

Fig. 9 and Fig. 10 respectively show the experimental results of TGCIs and VSGs with different parameters. When SCR is decreased from 11 to 4, the TGCI oscillates; however, when SCR is further decreased to 1, the VSG still operates stably. When the number of TGCIs is increased from one to two, the system begins to oscillate; however, when the number of VSGs is increased to three, the VSG does not oscillate. When the PLL bandwidth of the TGCI is increased to 400 Hz, the system oscillates. Therefore, the VSG shows better grid-connected stability than the TGCI.

VI. Conclusions

In this letter, the small-signal sequence impedance model of the VSG is built. By using the impedance-based approach, the grid-connected stability of the VSG and the TGCI is compared. The sequence impedance of the VSG is basically inductive; this is consistent with the impedance characteristics of the inductive grid. Under an ultra-weak grid or high penetration of renewable energy generation, the VSG grid-connected system can still run stably without PLL restrictions. From a system stability viewpoint, the VSG is more suitable than the TGCI for achieving high penetration of renewable energy generation in an ultra-weak grid.

Appendix

The typical control method of the TGCI is shown in Fig. 11. The control parameters of the TGCI are shown in Table II.

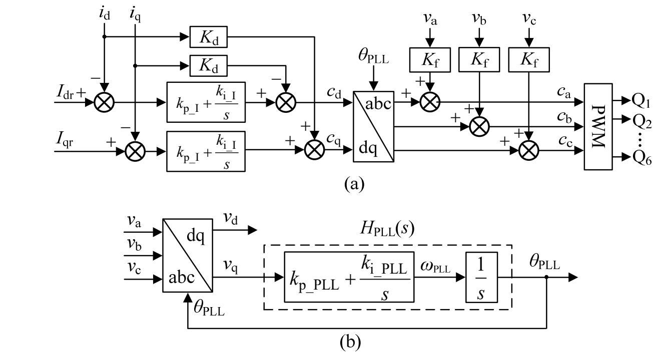

Fig. 11 Control scheme of the TGCI. (a) The output current feed-forward decoupling control; (b) The PLL in SRFs.

Table II. Control Parameters of the TGCI

Parameters	Values	Parameters	Values	Parameters	Values
k_{p_PLL}	0.2659	k_{p_I}	0.0343	K_f	0.0029
k_{i_PLL}	10.9988	k_{i_I}	45.7143	K_d	0.0027

References

[1] J. Sun, M. Li, Z. Zhang, T. Xu, J. He, H. Wang, and G. Li, "Renewable energy transmission by HVDC across the continent: system challenges and opportunities," *CSEE Journal of Power and Energy Systems*, vol. 3, no. 4, pp. 0-11, Dec. 2017.

[2] B. Wen, D. Dong, D. Boroyevich, and R. Burgos, "Impedance-based analysis of grid-synchronization stability for three-phase paralleled converters," *IEEE Trans. Power Electron*., vol. 31, no. 1, pp. 26-38, Jan. 2016.

[3] M. Cespedes, and J. Sun, "Impedance modeling and analysis of grid-connected voltage-source converters," *IEEE Trans. Power Electron*., vol. 29, no. 3, pp. 1254-1261, Mar. 2014.

[4] H. Liu, and J. Sun, "Voltage stability and control of offshore wind farms with AC collection and HVDC transmission," *IEEE J. Emerg. Sel. Topics Power Electron*., vol. 2, no. 4, pp. 1181-1189, Dec. 2014.

[5] K Alawasa, Y Mohamed, and W Xu, "Active mitigation of subsynchronous interactions between PWM voltage-source converters and power networks," *IEEE Trans. Power Electron*., vol. 29, no. 1, pp. 121-134, Jan. 2014.

[6] K. Alawasa, and Y. Mohamed, "Impedance and damping characteristics of grid-connected VSCs with power synchronization control strategy," *IEEE Trans. Power Syst*., vol. 30, no. 2, pp. 952-961, Mar. 2015.

[7] A. Egea-Alvarez, S. Fekriasl, F. Hassan, and O. Gomis-Bellmunt, "Advanced vector control for voltage source converters connected to weak grids," *IEEE Trans. Power Syst*., vol. 30, no. 6, pp. 3072-3081, Nov. 2015.

[8] Q. Zhong, and G. Weiss, "Synchronverters: inverters that mimic synchronous generators," *IEEE Trans. Ind. Electron*., vol. 58, no. 4, pp. 1259-1267, Apr. 2011.

[9] Q. Zhong, "Power-electronics-enabled autonomous power systems: architecture and technical routes," *IEEE Trans. Ind. Electron*., vol. 64, no. 7, pp. 5907-5918, Jul. 2017.

This article has been accepted for publication in a future issue of this journal, but has not been fully edited. Content may change prior to final publication. Citation information: DOI 10.1109/TPEL.2018.2841371, IEEE Transactions on Power Electronics

[10] H. Wu, X. Ruan, D. Yang, X. Chen, W. Zhao, Z. Lv, et al. “Small-signal modeling and parameters design for virtual synchronous generators,” *IEEE Trans. Ind. Electron.*, vol. 63, no. 7, pp. 4292-4303, Jul, 2016.

[11] Y. Du, J. M. Guerrero, L. Chang, J. Su, and M. Mao, “Modeling, analysis, and design of a frequency-droop-based virtual synchronous generator for microgrid applications,” in *Proceedings of ECCE Asia*, Melbourne, Australia, Jun. 2013, pp.643-649.

[12] S. D'Arco, J. Suul, and O. Fosso, “Small-signal modeling and parametric sensitivity of a virtual synchronous machine,” in *Proc. IEEE PSCC Conf.*, Aug. 2014, pp. 1-9.

[13] C. Hu, K. Chen, S. Luo, B. Zhou, and L. Ding, “Small signal modeling and stability analysis of virtual synchronous generators,” in *Proc. IEEE ICEMS Conf.*, Aug. 2017, pp. 1-5.

[14] L. Harnefors, A. Yepes, A. Vidal, and J. Doval-Gandoy, “Passivity-based controller design of grid-connected VSCs for prevention of electrical resonance instability,” *IEEE Trans. Ind. Electron.*, vol. 62, no. 2, pp. 702-710, Feb. 2015.

[15] J. Sun, “Impedance-based stability criterion for grid-connected inverters,” *IEEE Trans. Power Electron.*, vol. 26, no. 11, pp. 3075-3078, Nov. 2011.